Journal of Power Sources 243 (2013) 280–289

Contents lists available at SciVerse ScienceDirect

Journal of Power Sources

journal homepage: www.elsevier.com/locate/jpowsour

Transient three-dimensional thermal model for batteries with thin electrodes

Peyman Taheri, Maryam Yazdanpour, Majid Bahrami*

Laboratory for Alternative Energy Conversion (LAEC), Mechatronic Systems Engineering, School of Engineering Science, Simon Fraser University, Surrey, BC V3T 0A3, Canada

HIGHLIGHTS

- A three-dimensional transient thermal model is proposed to investigate batteries thermal behavior.
- Orthotropic properties and transient heat generation inside the battery core are considered.
- The model uses integral transformation method with minimum computational effort.
- The model allows to apply convective–radiative boundary conditions for the battery.
- Application of the proposed method is demonstrated for a sample lithium-ion.

ARTICLE INFO

Article history:
Received 19 March 2013
Accepted 24 May 2013
Available online 11 June 2013

Keywords:
Battery thermal management
Battery thermal response
Analytical thermal model
Integral-transformation technique
Lithium-ion battery

ABSTRACT

A three-dimensional analytical model is proposed to investigate the thermal response of batteries, with a plurality of thin electrodes, to heat generation during their operation. The model is based on integral-transform technique that gives a closed-form solution for the fundamental problem of unsteady heat conduction in batteries with orthotropic thermal conductivities, where the heat generation is a function of both temperature and depth-of-discharge. The full-field solutions take the form of a rapidly converging triple infinite sum whose leading terms provide a very simple yet accurate approximation of the battery thermal behavior with modest numerical effort. The accuracy of the proposed model is tested through comparison with numerical simulations. The method is used to describe spatial and temporal temperature evolution in a sample pouch type lithium-ion polymer battery during galvanostatic discharge processes while subjected to convective–radiative cooling at its surfaces (the most practical case is considered, when surrounding medium is at a constant ambient temperature). In the simulations, emphasis is placed on the maintenance of the battery operational temperature below a critical temperature. Through definition of a surface-averaged Biot number, certain conditions are highlighted, under which a two-dimensional thermal analysis is applicable.

1. Introduction

Batteries with thin porous-electrode assemblies are well-known for their high columbic efficiency. Among different types of rechargeable batteries with thin porous electrodes, lithium-ion (Li-ion) polymer cells have become very popular due to their high specific energy (~180 Wh kg^{-1}), high energy density (~400 Wh L^{-1}), high operating voltage (up to about 4 V), short charging time, minimal memory effects and low self-discharge rate (around 5–8% per month), and long cycling life [1]. Such desired features have made Li-ion batteries one the most favored candidates for portable energy storage systems, and they are already replacing nickel–metal hydride (NiMH) batteries.

More recently, the strategy of electrifying vehicles with high-capacity batteries in order to reduce or remove the contribution of internal combustion engine into the powertrain has attracted an intense attention. Nevertheless, the persisting challenge associated with large-scale application of batteries in hybrid-electric and plug-in electric vehicles (H/PEVs) is their temperature control. For example, it is evident that during severe discharge conditions, which involve high rates of exothermic electrochemical reactions and Joule heating, Li-ion batteries are prone to excessive temperature rise that can initiate swelling [2], thermal runaway [3,4], electrolyte fire, and in extreme cases explosion [5]. Moreover, exposure of Li-ion batteries to sub-freezing temperatures drastically reduces their energy and power delivery [6]. As a result,

* Corresponding author.
E-mail addresses: ptaherib@sfu.ca (P. Taheri), myazdanp@sfu.ca (M. Yazdanpour), mbahrami@sfu.ca (M. Bahrami).

0378-7753/$ – see front matter © 2013 Elsevier B.V. All rights reserved.
http://dx.doi.org/10.1016/j.jpowsour.2013.05.175

design of an efficient "battery thermal management system (BTMS)" is crucial for batteries' safety, efficiency, and longevity.

An efficient BTMS is required to keep the batteries' temperature within a narrow range (for room temperature Li-ion batteries the ideal temperature range is 20–30 °C), and provide a minimum temperature variation within the battery pack, i.e., a uniform temperature distribution [7]. In order develop an effective BTMS, accurate thermal models are required to predict thermal response of the batteries under transient and dynamic load cycles [8,9].

The thermal behavior of batteries is strongly coupled to the rate of electro-chemical processes during charge and discharge cycles [10,11]; however, for large-scale battery assemblies, e.g., in hybrid and electric vehicles, collective behavior of electro-chemical processes, deduced from measurements, can be included as the heat source in a standalone thermal model. Based on this decoupling strategy, there are several battery thermal models available in the literature including one-dimensional [12], two-dimensional [13–15], and three-dimensional models [16–19], in which variety of cell designs, modes of operation, and thermophysical properties are considered. For an extensive bibliography on battery thermal models see Ref. [11].

Advanced thermal simulations for emerging batteries with laminated structure reveal that owing to their orthotropic thermal conductivities, a three-dimensional thermal model should be adapted to properly study thermal response of such batteries. To the author's best knowledge, all the multi-dimensional thermal models developed for such batteries rely on numerical solutions; thus, lack of a theoretical method is evident. The only available analytical solution is the work of Newman and Tiedemann [20], where the classical technique of separation of variables is employed to solve the transient heat conduction problem for batteries with a constant heat generation and constant-temperature boundary conditions. In this study, we investigate the same problem featuring transient heat generation and convective–radiative boundary conditions that yield a more realistic representation of the operating conditions for batteries used in applications such as H/PEVs. Furthermore, the method allows to take account for both reversible and irreversible heats generation rates, which are functions of temperature and depth-of-discharge, respectively. In our approach, since both the energy equation and boundary conditions involve non-homogeneities, the integral-transform technique [21,22] is used to obtain a closed-form solution for temperature field. Dictated by the type of boundary conditions, the presented thermal model may involve numerical calculations of eigenvalues. Accordingly, the model can be classified as a semi-analytic model or just an analytic model; while in this paper, the authors refer to the model as "analytical" since it yields a closed-form solution.

In the following sections, the theoretical thermal model is explained, and its application to investigate the thermal response of a sample pouch type Li-ion polymer battery during galvanostatic discharge processes is demonstrated. Evolution of the temperature field in the battery is discussed for different discharge rates and various convective–radiative cooling conditions at its surfaces. Results from the proposed analytical model are compared to numerical data, which exhibit a good agreement. Although the method is implemented for discharging a Li-ion cell, its generality allows to use it for investigating thermal behavior and BTMS design of batteries with different chemistries which use laminated architecture in their electrodes.

2. Formulation of the problem

We consider a three-dimensional rectangular orthotropic solid of length L_1, width L_2, and height L_3, which represents the core of a battery. For better reading, a two-dimensional schematic of the domain is shown in Fig. 1. Heat is generated non-uniformly within the domain, while heat transfer with a surrounding medium is allowed at boundary surfaces.

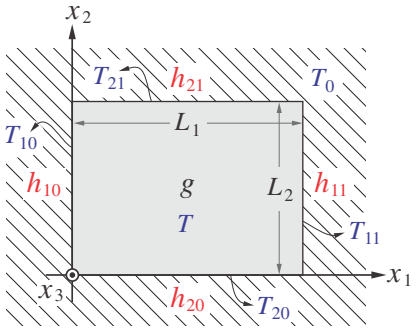

Fig. 1. Two-dimensional schematic of a solid domain with internal heat generation, and heat dissipation at boundaries. The ambient and initial temperatures are T_0.

The unsteady temperature distribution inside the domain is described by a three-dimensional energy balance equation which only includes conduction terms,

$$\rho c_p \frac{\partial T}{\partial t} = \kappa_1 \frac{\partial^2 T}{\partial x_1^2} + \kappa_2 \frac{\partial^2 T}{\partial x_2^2} + \kappa_3 \frac{\partial^2 T}{\partial x_3^2} + g, \quad 0 \le x_1 \le L_1, \quad 0 \le x_2 \le L_2, \quad 0 \le x_3 \le L_3, \quad t > 0, \tag{1}$$

in which t is time, and $\mathbf{x} = \{x_1, x_2, x_3\}$ represents the components of position vector in Cartesian coordinate system. The density ρ, heat capacity per unit mass c_p, and orthotropic thermal conductivity vector $\boldsymbol{\kappa} = \{\kappa_1, \kappa_2, \kappa_3\}$ are the thermophysical parameters. The functions $T(\mathbf{x},t)$ and $g(\mathbf{x},t)$ represent the temperature and volumetric heat generation rate, respectively.

It should be noted that in derivation of Eq. (1), the thermophysical properties are assumed to be independent of temperature, which is generally acceptable over a reasonably narrow temperature range of interest (i.e., the desired operating temperature range for batteries). This is a key assumption which leads to a linear energy balance equation [cf. Eq. (1)] and makes an analytical solution feasible.

A convective thermal boundary condition at the boundaries of the domain is applied. Convective heat fluxes at domain surfaces are,

$$q_{c,ij} = h_{c,ij}(T_{ij} - T_0), \quad (i = 1,2,3;\ j = 0,1), \tag{2}$$

where $h_{c,ij}$ are convective heat transfer coefficients at different boundaries, and T_{ij} are the corresponding surface temperatures. The environment temperature T_0 is assumed to be a constant. The index i represents the direction of the normal vector on a boundary surface, while $j = 0$ and $j = 1$ denote surfaces at $x_i = 0$ and $x_i = L_i$, respectively (see Fig. 1).

The initial temperature of the domain is the same as environment temperature T_0,

$$T = T_0, \quad \text{at } t = 0. \tag{3}$$

In this study, we consider constant ambient temperatures; however, the method allows definition of ambient temperatures as a function of both space and time [21,22].

Similar to analyses in Refs. [16,17,19], the effects of radiative heat dissipation can be included in the thermal model. The radiative heat flux reads,

$$q_{r,ij} = \varepsilon\sigma\left(T_{ij}^4 - T_0^4\right), \quad (i = 1,2,3;\ j = 0,1), \tag{4}$$

where ε is the emissivity of the surface and σ is the Stefan–Boltzmann constant. The boundary condition in Eq. (4) is nonlinear since it contains the forth power of the unknown surface temperature T_{ij}. However, if $|T_{ij} - T_0|/T_0 \ll 1$, Eq. (4) can be linearized and takes the form [21],

$$q_{r,ij} = 4\varepsilon\sigma T_0^3 (T_{ij} - T_0) = h_r (T_{ij} - T_0), \quad (i = 1,2,3;\ j = 0,1), \tag{5}$$

in which $h_r = 4\varepsilon\sigma T_0^3$ is the heat transfer coefficient for radiation.

Combination of convective and radiative heat transfer coefficients leads to the following general boundary conditions for Eq. (1),

$$-\kappa_i \frac{\partial T}{\partial x_i} + h_{i0}(T_{i0} - T_0) = 0, \quad \text{at } x_i = 0 \quad (i = 1,2,3), \tag{6a}$$

$$+\kappa_i \frac{\partial T}{\partial x_i} + h_{i1}(T_{i1} - T_0) = 0, \quad \text{at } x_i = L_i \quad (i = 1,2,3), \tag{6b}$$

with $h_{i0} = h_{c,i0} + h_r$ and $h_{i1} = h_{c,i1} + h_r$ as combined convective–radiative heat transfer coefficients, that will be referred as 'heat transfer coefficient' in the rest of the paper.

To complete our definition of the initial-boundary-value problem, volumetric heat generation rate $g(\mathbf{x},t)$ inside the battery should be determined. Indeed, one of the most challenging tasks in thermal modeling of batteries is the evaluation of local heat generation rate during charge/discharge processes. Complexities associated with this task are rooted in the strong coupling of heat generation rate to chemical reactions rate and local Joule heating effects inside the battery structure [10,23,24].

Bernardi et al. [25] proposed a general energy balance equation for battery thermal models in which the heat generation rate is approximated as,

$$g = \pm \frac{I}{\mathscr{V}} \left[(V - V_{oc}) + T \frac{dV_{oc}}{dT} \right], \tag{7}$$

with positive and negative signs for charge and discharge processes, respectively. The above equation is accurate enough to perform thermal analysis for battery systems regardless of detailed electro-chemical processes [19], if the value of dV_{oc}/dT is known from electro-chemical simulations. The parameters I and V denote operational current and voltage of the battery, and $\mathscr{V}$ is the battery volume. Open circuit potential (OCP) of the battery, also known as equilibrium potential, is denoted by V_{oc}. The term $I(V - V_{oc})/\mathscr{V}$ is the irreversible heat generation due to cell overpotential (electrodes polarization) and ohmic potential drop. The term $IT(dV_{oc}/dT)/\mathscr{V}$ is the reversible heat caused by the entropy change of electro-chemical reactions [25,26]. In this study we assume that open circuit potential V_{oc} linearly depends on temperature [19], that is, $dV_{oc}/dT = \text{constant}$.

The fact should be highlighted that hot spots can be established in batteries, particularly in the vicinity of battery terminals, as a result of electrical constriction resistances [15,27,28]. In order to accommodate the actual heat generation in the present model, it must be coupled to an electrical model.

3. Analytical solution

The system of initial-boundary-value problem, described with Eqs. (1), (3), (6) and (7) can be transformed into a more convenient form, by defining the dimensionless space and time as,

$$\xi_i = \frac{x_i}{L_i} \quad (i = 1,2,3), \quad \tau = \frac{\kappa_1/L_1^2}{\rho c_p/t}. \tag{8}$$

where κ_i/L_i^2 in x_1 direction is arbitrarily used to define the dimensionless time. Rewriting Eqs. (1), (3) and (6) in terms of dimensionless quantities gives,

$$\frac{\partial\theta}{\partial\tau} = \frac{\partial^2\theta}{\partial\xi_1^2} + K_2\frac{\partial^2\theta}{\partial\xi_2^2} + K_3\frac{\partial^2\theta}{\partial\xi_3^2} + G, \quad 0 \le \xi_1 \le 1, \quad 0 \le \xi_2 \le 1, \quad 0 \le \xi_3 \le 1, \quad \tau > 0, \tag{9}$$

with boundary conditions,

$$-\frac{\partial\theta}{\partial\xi_i} + \mathrm{Bi}_{i0}\theta_{i0} = 0, \quad \text{at } \xi_i = 0 \quad (i = 1,2,3), \tag{10a}$$

$$+\frac{\partial\theta}{\partial\xi_i} + \mathrm{Bi}_{i1}\theta_{i1} = 0, \quad \text{at } \xi_i = 1 \quad (i = 1,2,3), \tag{10b}$$

and the initial condition,

$$\theta = 0, \quad \text{at } \tau = 0. \tag{11}$$

In Eq. (9), K_i are the dimensionless orthotropic thermal conductivities, and in the transformed boundary conditions [cf. Eq. (10)] Bi_{ij} are Biot numbers,

$$K_i = \frac{\kappa_i/L_i^2}{\kappa_1/L_1^2} \quad (i = 1,2,3), \quad \mathrm{Bi}_{ij} = \frac{h_{ij}L_i}{\kappa_i} \quad (i = 1,2,3;\ j = 0,1), \tag{12}$$

The temperature rise inside the domain is denoted by θ, and the temperature rise on the boundaries is θ_{ij},

$$\theta = T - T_0, \quad \theta_{ij} = T_{ij} - T_0. \tag{13}$$

The source for temperature rise G (in temperature unit) is,

$$G = \frac{g}{\kappa_1/L_1^2} = \pm G_{\text{irrev}} \pm G_{\text{rev}} \pm G_0, \tag{14a}$$

with positive and negative signs for charge and discharge processes, respectively. The terms in Eq. (14a) and the positive constant α are,

$$G_{\text{irrev}} = \alpha(V - V_{oc}), \quad G_{\text{rev}} = \alpha\theta\frac{dV_{oc}}{d\theta}, \quad G_0 = \alpha T_0\frac{dV_{oc}}{d\theta}, \quad \text{and} \quad \alpha = \frac{I/\mathscr{V}}{\kappa_1/L_1^2}. \tag{14b}$$

During battery operation $V - V_{oc}$ varies with time, thus, the irreversible heat generation term is an explicit function of time, $G_{\text{irrev}} = G_{\text{irrev}}(\tau)$. Quite differently, the entropic (reversible) heat generation term explicitly depends on temperature (rise) and implicitly depends on time via temperature, i.e., $G_{\text{rev}} = G_{\text{rev}}(\theta)$. Note that we assumed $dV_{oc}/d\theta$ is a constant, then, G_0 turns out to be a constant reversible heat generation corresponding to the initial temperature T_0.

The transformed system [cf. Eqs. (9)–(11)] that describes the temperature rise with respect to the dimensionless space and time, is solved analytically using a finite-integral transform technique, as described below.

The triple integral transformation and the inversion formula for temperature function are defined as [21],

$$\overline{\theta}(\lambda_{1l},\lambda_{2m},\lambda_{3n},\tau) = \int_{\xi_1'=0}^{1}\int_{\xi_2'=0}^{1}\int_{\xi_3'=0}^{1} \psi(\lambda_{1l},\xi_1')\cdot\psi(\lambda_{2m},\xi_2') \cdot\psi(\lambda_{3n},\xi_3')\cdot\theta(\xi_1',\xi_2',\xi_3',\tau)\cdot \mathrm{d}\xi_1'\cdot\mathrm{d}\xi_2'\cdot\mathrm{d}\xi_3', \tag{15}$$

and,

$$\theta(\xi_1,\xi_2,\xi_3,\tau) = \sum_{l=1}^{\infty}\sum_{m=1}^{\infty}\sum_{n=1}^{\infty}\psi(\lambda_{1l},\xi_1)\cdot\psi(\lambda_{2m},\xi_2) \cdot\psi(\lambda_{3n},\xi_3)\cdot\overline{\theta}(\lambda_{1l},\lambda_{2m},\lambda_{3n},\tau). \tag{16}$$

The functions $\psi(\lambda_{1l},\xi_1)$, $\psi(\lambda_{2m},\xi_2)$, and $\psi(\lambda_{3n},\xi_3)$ are the transformation kernels (normalized eigenfunctions) in ξ_1, ξ_2, and ξ_3 directions,

$$\psi(\lambda_i,\xi_i) = \frac{\phi(\lambda_i,\xi_i)}{\eta_i^{1/2}} \quad (i = 1,2,3), \tag{17}$$

and $\phi(\lambda_i,\xi_i)$ are the eigenfunctions,

$$\phi(\lambda_i,\xi_i) = \cos(\lambda_i\xi_i) + \frac{\mathrm{Bi}_{i0}}{\lambda_i}\sin(\lambda_i\xi_i) \quad (i = 1,2,3), \tag{18}$$

The eigenfunctions are solutions of the following Sturm–Liouville system corresponding to Eqs. (9) and (10),

$$\frac{\mathrm{d}^2\phi}{\mathrm{d}\xi_i^2} + \lambda_i^2\phi = 0 \quad (i = 1,2,3), \tag{19a}$$

$$-\frac{\mathrm{d}\phi}{\mathrm{d}\xi_i} + \mathrm{Bi}_{i0}\phi = 0, \quad \text{at } \xi_i = 0 \quad (i = 1,2,3), \tag{19b}$$

$$+\frac{\mathrm{d}\phi}{\mathrm{d}\xi_i} + \mathrm{Bi}_{i1}\phi = 0, \quad \text{at } \xi_i = 1 \quad (i = 1,2,3), \tag{19c}$$

In Eqs. (17)–(19), λ_i denotes an infinite list of eigenvalues in ξ_i direction. In Eqs. (15) and (16) components of λ_i in ξ_1, ξ_2, and ξ_3 directions are denoted by λ_{1l}, λ_{2m}, and λ_{3n}, respectively. The subscripts l, m, and n are the indices for the list components. The eigenvalues in each direction are positive roots of the following transcendental equation [21],

$$\tan\lambda = \frac{\lambda(\mathrm{Bi}_{i0}+\mathrm{Bi}_{i1})}{\lambda^2 - \mathrm{Bi}_{i0}\mathrm{Bi}_{i1}}, \quad (i = 1,2,3). \tag{20}$$

Eigenvalues normalization factors η_i, which appears in Eq. (17), are obtained as [21],

$$\eta_i = \frac{1}{2}\left[\frac{\lambda_i^2+\mathrm{Bi}_{i0}^2}{\lambda_i^2}\left(1+\frac{\mathrm{Bi}_{i1}}{\lambda_i^2+\mathrm{Bi}_{i1}^2}\right) + \frac{\mathrm{Bi}_{i0}}{\lambda_i^2}\right], \quad (i = 1,2,3). \tag{21}$$

The integral transform of Eq. (9), according to transformation (15), yields the following ordinary differential equation for $\overline{\theta}$,

$$\frac{\mathrm{d}\overline{\theta}}{\mathrm{d}\tau} + \Delta_{lmn}\overline{\theta} = \pm\overline{G}_{\mathrm{irrev}} \pm \overline{G}_0, \quad \text{with } \overline{\theta}(\tau) = 0 \quad \text{at } \tau = 0. \tag{22a}$$

in which,

$$\Delta_{lmn} = \lambda_{1l}^2 + K_2\lambda_{2m}^2 + K_3\lambda_{3n}^2 \mp \alpha\frac{\mathrm{d}V_{\mathrm{oc}}}{\mathrm{d}\theta}. \tag{22b}$$

Note that in Eq. (22a) positive signs are applied for charging and negative signs for discharging, whereas in Eq. (22b) the negative sign is applicable for charging and the positive sign for discharging. Quantities with a bar refer to transformed quantities as given by Eq. (15), i.e.,

$$\begin{pmatrix}\overline{G}_{\mathrm{irrev}}(\lambda_{1l},\lambda_{2m},\lambda_{3n},\tau)\\ \overline{G}_0\ (\lambda_{1l},\lambda_{2m},\lambda_{3n},\tau)\end{pmatrix} = \int_{\xi_1'=0}^{1}\int_{\xi_2'=0}^{1}\int_{\xi_3'=0}^{1}\psi(\lambda_{1l},\xi_1') \cdot\psi(\lambda_{2m},\xi_2')\cdot\psi(\lambda_{3n},\xi_3')\cdot\begin{pmatrix}G_{\mathrm{irrev}}(\xi_1',\xi_2',\xi_3',\tau)\\ G_0(\xi_1',\xi_2',\xi_3',\tau)\end{pmatrix}\cdot\mathrm{d}\xi_1'\cdot\mathrm{d}\xi_2'\cdot\mathrm{d}\xi_3', \tag{22c}$$

Equation (22a) is a first-order, linear, and inhomogeneous ODE with a constant coefficient, Δ_{lmn}. Its solution $\overline{\theta}(\lambda_{1l},\lambda_{2m},\lambda_{3n},\tau)$ can be obtained as,

$$\overline{\theta} = \exp(-\Delta_{lmn}\tau)\left[\int_{\tau}\exp(\Delta_{lmn}\tau)\left(\pm\overline{G}_{\mathrm{irrev}}(\tau)\pm\overline{G}_0\right)\mathrm{d}\tau + \mathscr{C}\right], \tag{23}$$

for which the corresponding integrating constant $\mathscr{C}$ must be evaluated from the given initial condition, $\overline{\theta}(\lambda_{1l},\lambda_{2m},\lambda_{3n},0) = 0$. Substitution of this solution into the inversion formula (16) gives the final solution in series form.

In Eqs. (15) and (16), if a double integral and its corresponding summation are defined (instead of the triple ones), a two-dimensional solutions can be obtained by following the presented procedure.

4. Results and discussions

In this section, thermal behavior of a sample lithium-ion pouch cell during discharge processes is investigated using the proposed analytical approach. The required calculations, as presented in Section 3, are programmed symbolically in Mathematica© to obtain a generic solution in series form, i.e., Eq. (16). The details of the model implementation are discussed in Appendix A.

It should be noted that compared to the existing multi-dimensional numerical approaches, e.g. Refs. [12–14,16–19,28], our analytical model demands minimum numerical effort, which is required for evaluation of eigenvalues from the transcendental equation [cf. Eq. (20)].

4.1. Structure and thermophysical properties of the sample lithium-ion polymer battery

Pouch type (prismatic) lithium-ion polymer batteries use specific battery architecture; the liquid lithium-salt electrolyte is held within the multi-layered porous structures of electrodes and separator sheets, which are made of solid polymer composites. Application of porous electrodes promotes intimate contact of the electrode material with the electrolyte solution, leading to higher rate of electrochemical reactions. Fig. 2(a) schematically shows the internal multi-layered structure of a prismatic polymer Li-ion battery, in which negative and positive porous electrodes are alternatively wrapped in separator sheets. A battery core as shown in Fig. 2(b), includes several layers of electrodes and separators enclosed in a case (the case is not shown). A unit cell of the battery layered arrangement is depicted in Fig. 2(c), in which lithium ions Li^+ are transporting from anode to cathode during a discharge process.

In order to demonstrate how to apply the proposed thermal model to batteries, ePLB C020 battery fabricated by EiG Corporation (South Korea) is considered as our sample battery. This battery uses Li[Ni Co Mn_2]O_2 and graphite as active materials at cathode and

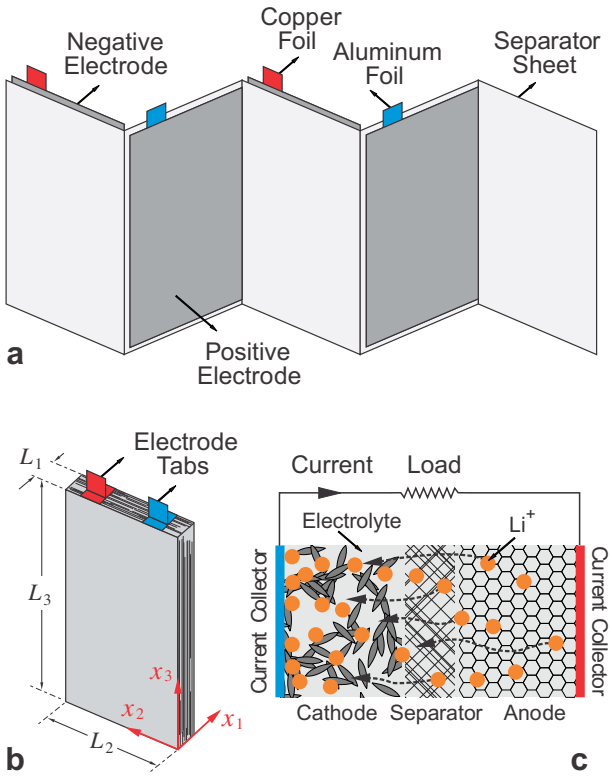

Fig. 2. (a) Multi-layered core configuration in a prismatic lithium-ion polymer battery; (b) core of a single battery pack (the battery case is not shown); (c) a unit cell of the battery including a pair of porous electrodes, a porous separator, and current collectors is shown during discharge process. The pores of polymer components, i.e., electrodes and separator are filled with an electrolyte liquid which allows transfer of ions between the electrodes.

anode, respectively. The nominal voltage and capacity of the battery are 3.65 V and 20 Ah, with specific energy of 175 Wh kg^{-1}. The weight of the battery is approximately 407 g, thus, its energy content is approximately 71 Wh. Mechanical and electrical specifications of the battery are listed in Table 1.

The sample battery includes 18 negative electrodes, 17 positive electrodes, and 36 layers of polymer (polypropylene) separator sheets. The electrodes which include current collector foils laminated by thin layers of a polymer (polyethylene oxide) are connected in parallel. Aluminum and copper foils are used as current collectors in positive and negative electrodes, respectively. The polymer layers (electrodes and separator sheets) are porous media soaked in an electrolyte liquid (a mixture of ethylene carbonate and dimethyl carbonate) and accommodate active materials required in the battery chemistry. The battery core [Fig. 2(a)] is packed in a polymer laminate aluminum pouch case. The thickness and thermophysical properties of the battery core layers/materials are provided in Table 2. Density, heat capacity, and thermal conductivity of porous polymer layers in the electrodes and separator sheets must be measured after they are soaked in the electrolyte liquid. Since heat capacity and thermal conductivity of battery components are not reported by the manufacturer, we use available data in the literature for a similar battery type [15,19,27].

Due to small thickness of porous polymers and presence of impermeable foils in the battery structure, the mobility of electrolyte is negligible, and as given in Eq. (1), conduction is the dominant mechanism for heat transfer inside the battery core.

In order to solve Eqs. (9)–(11), it is necessary to determine the thermophysical parameters within the battery core. To avoid

Table 1
Specifications of ePLB C020, EiG battery.

Mechanical characteristics	
Thickness (L_1)	7 [mm]
Width (L_2)	125 [mm]
Height (L_3)	195 [mm]
Weight	407 [g]
Electrical characteristics	
Nominal voltage	3.65 [V]
Nominal capacity	20 [Ah]
Specific energy	175 [Wh kg^{-1}]
Energy density	370 [Wh L^{-1}]
Specific power (DOD 50%, 10 s)	2300 [W kg^{-1}]
Power density (DOD 50%, 10 s)	4600 [W L^{-1}]
Operating conditions	
Recommended voltage limit for discharge	3 [V]
Lower voltage limit for discharge	2.5 [V]
Maximum continuous discharge current	5C
Maximum discharge current (peak<10 s)	10C
Operating temperature	Between −30 °C and +50 °C
Recommended charge temperature	Between 0 °C and +40 °C

complexities associated with multi-material multi-layered structure of the battery [cf. Fig. 2] we use averaged/effective transport properties in this study.

The product value of density and heat capacity can be averaged based on density, heat capacity, and volume of each layer (component) [11,19],

$$\rho c_p = \frac{\sum_{j=1}^{N} \rho_j c_{p,j} \mathscr{V}_j}{\mathscr{V}} = 2767.45 \left[\mathrm{kJ/m^3 K}\right], \tag{24}$$

for which the required data are provided in Tables 1 and 2. The quantity $\mathscr{V}$ is the total battery volume, $\mathscr{V}_j$ is the volume of the jth component (layer), and N is the total number of components (layers). Furthermore, the concept of *equivalent resistance network* can be employed to define effective thermal conductivity in different directions. Based on Fig. 2, there are series thermal resistors in x_1 direction and parallel thermal resistors in x_2 and x_3 directions. Accordingly, by using the data from Tables 1 and 2, through-plane and in-plane orthotropic conductivities are evaluated as [9,11,19],

$$\kappa_1 = \frac{\sum_{j=1}^{N} \ell_j}{\sum_{j=1}^{N} (\ell_j/\kappa_j)} = 0.97[\mathrm{W/m\,K}], \quad \text{and} \quad \kappa_2 = \kappa_3 = \frac{\sum_{j=1}^{N} \ell_j \kappa_j}{\sum_{j=1}^{N} \ell_j} = 26.57[\mathrm{W/m\,K}], \tag{25}$$

where ℓ_j denotes the thickness of the jth component (layer) in x_1 direction, and $\sum_{j=1}^{N} \ell_j = L_1$.

It must be emphasized that as a consequence of laminated arrangement of the battery core, interfacial phenomena of contact resistance at porous–porous and porous–solid interfaces must be considered in evaluation of effective thermal conductivities.

Table 2
Thickness and thermophysical properties of battery components.

Material/layer	Thickness [μm]	Number of layers	Density [kg m^{-3}]	Heat capacity [J kg^{-1} K^{-1}]	Thermal conductivity [W m^{-1} K^{-1}]
Aluminum foil	21	17	2702	903	238
Copper foil	12	18	8933	385	398
Separator sheet	25	36	1017 (wet)	1978 (wet)	0.34 (wet)
Positive electrode	70	34	2895 (wet)	1270 (wet)	1.58 (wet)
Negative electrode	79	36	1555 (wet)	1437 (wet)	1.04 (wet)
Pouch (case)	162	2	1150	1900	0.16

However, for Li-ion polymer batteries, since the contact interfaces are wet at the presence of the electrolyte liquid, the effects of contact resistance are assumed to be negligible. This simplification is usually justified with the fact that thermal conductivities of electrolyte and polymer compounds are in the same order. Detailed experimental study on "internal contact resistance" in batteries is not available, and the authors believe that this important phenomenon is overlooked and plan to further investigate this potentially critical issue in depth. The effects of "external contact resistance" in large battery assemblies are discussed in Ref. [29].

The pouch case of the battery is made of polyethylene-laminated aluminum foil. As reported in Table 2, since the thickness of the pouch is small, 162 μm, and its through-plane thermal conductivity is not very different from the battery bulk (compare to κ_1 in Eq. (25)) its effect on bulk temperature has been excluded from the thermal analysis; however, in reality the pouch casing contributes as an insulation. For an accurate boundary treatment, the outer surface temperature of the case should be related to surface temperature of the battery core; see Refs. [16,17] for more precise boundary conditions.

4.2. Battery temperature distribution

The dimensions of the battery as given in Table 1 are chosen to be $L_1 = 0.007$ m, $L_2 = 0.125$ m, and $L_3 = 0.195$ m. The effective thermophysical properties of the battery core are evaluated from Eqs. (24) and (25). Experimental data, reported by EiG for its ePLB C020 cell, on variation of cell potential (voltage) versus depth-of-discharge (DOD) for different discharge rates are shown in Fig. 3(a). For discharge processes, based on the recommended voltage limit in Table 1, the cut-off voltage of 3 V is considered. Heat generation rate inside the battery is approximated from Eq. (7). Since the capacity of the sample battery is 20 Ah, the empirical data for $C/2$, $1C$, $2C$, $3C$, and $5C$ discharge rates, as shown in Fig. 3(b), correspond to 10 A, 20 A, 40 A, 60 A, and 100 A discharge currents, during 2 h, 1 h, 30 min, 20 min, and 12 min, respectively. In Fig. 3(b), variations of open-circuit and operating voltages at different discharge currents are plotted versus dimensionless time τ, where in account for Eq. (8), $t = 139.8\,\tau$.

For different discharge modes, summation of irreversible heat generation $G_{\text{irrev}}(\tau)$ and the constant heat generation G_0 are plotted in Fig. 4 for $T_0 = 25$ °C. The term $V - V_{\text{oc}}$ is evaluated by fitting fifth-order polynomials to the data points in Fig. 3(b), and using Eq. (14b). Linear transformations in (8) and (14a) can be used to relate the magnitude of G to g, which in our case is $g = 19{,}796G$. The sharp increase in heat generation at the end of discharge corresponds to large differences between OCP and operating voltages.

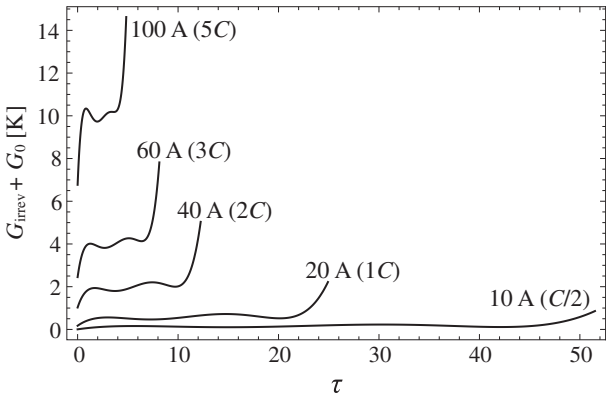

Fig. 4. Variation of $G_{\text{irrev}} + G_0$ vs. dimensionless time τ is shown for different discharge currents at 25 °C.

Battery thermal management systems operate based on heat transfer at battery surfaces, and their design depends on a variety of parameters, including: *i*) thermal management strategy, that can be either active or passive [30] or a combination; *ii*) the type of the coolant (gas or liquid); *iii*) coolant circulation design (flow passage area, laminar or turbulent flow, etc); *iv*) the size and the shape of the battery assembly; *v*) recommended operational temperature for the battery, to name a few. We assume small and moderate heat transfer coefficients to investigate the possibility of natural and forced convection cooling with air. The ambient and initial temperatures are assumed to be $T_0 = 298.15$ K, thus, based on the recommended operation temperature in Table 1, the maximum temperature rise of $\theta = 25$ K is acceptable during the battery operation, which means the critical temperature is $T_{\text{Cri}} = 323.15$ K. Here, only discharge operation mode is considered, but the same method can be used for charging process if variations of OCP and operation voltage are given during charging period.

Variation of maximum temperature T_{Max} at the center of the battery $\xi = (0.5, 0.5, 0.5)$, minimum temperature T_{Min} at the corner of the battery $\xi = (0, 0, 0)$, and averaged battery temperature T_{Ave} as a function of battery utilization (DOD) are shown in Fig. 5. The average temperature is calculated as,

$$T_{\text{Ave}} = T_0 + \int_{\xi_1=0}^{1}\int_{\xi_2=0}^{1}\int_{\xi_3=0}^{1} \theta(\xi_1, \xi_2, \xi_3, \tau)\,\mathrm{d}\xi_1\mathrm{d}\xi_2\mathrm{d}\xi_3. \qquad (26)$$

The temperatures T_{Max}, T_{Min}, and T_{Ave} obtained from the proposed analytical model for different discharge modes and heat transfer

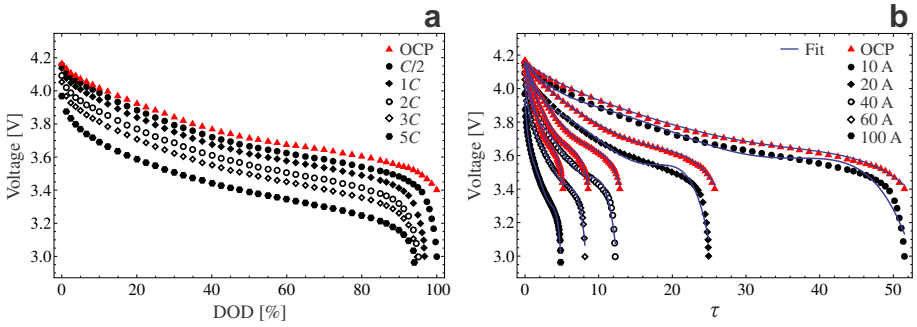

Fig. 3. (a) Experimental data reported by EiG Corp. on variation of battery voltage versus depth-of-discharge (DOD) at 25 °C for different discharge conditions in C-rate. A $1C$-rate means that the current completely discharges the battery in 1 h. The red triangle symbols (▲) represent open circuit potential (OCP); (b) variation of open circuit potential (OCP) and operation voltage of the battery versus dimensionless time τ ($t = 139.8\tau$ s), for different discharge currents. Solid lines in plot (b) represent fifth-order polynomial fits to the experimental data. (For interpretation of the references to color in this figure legend, the reader is referred to the web version of this article.)

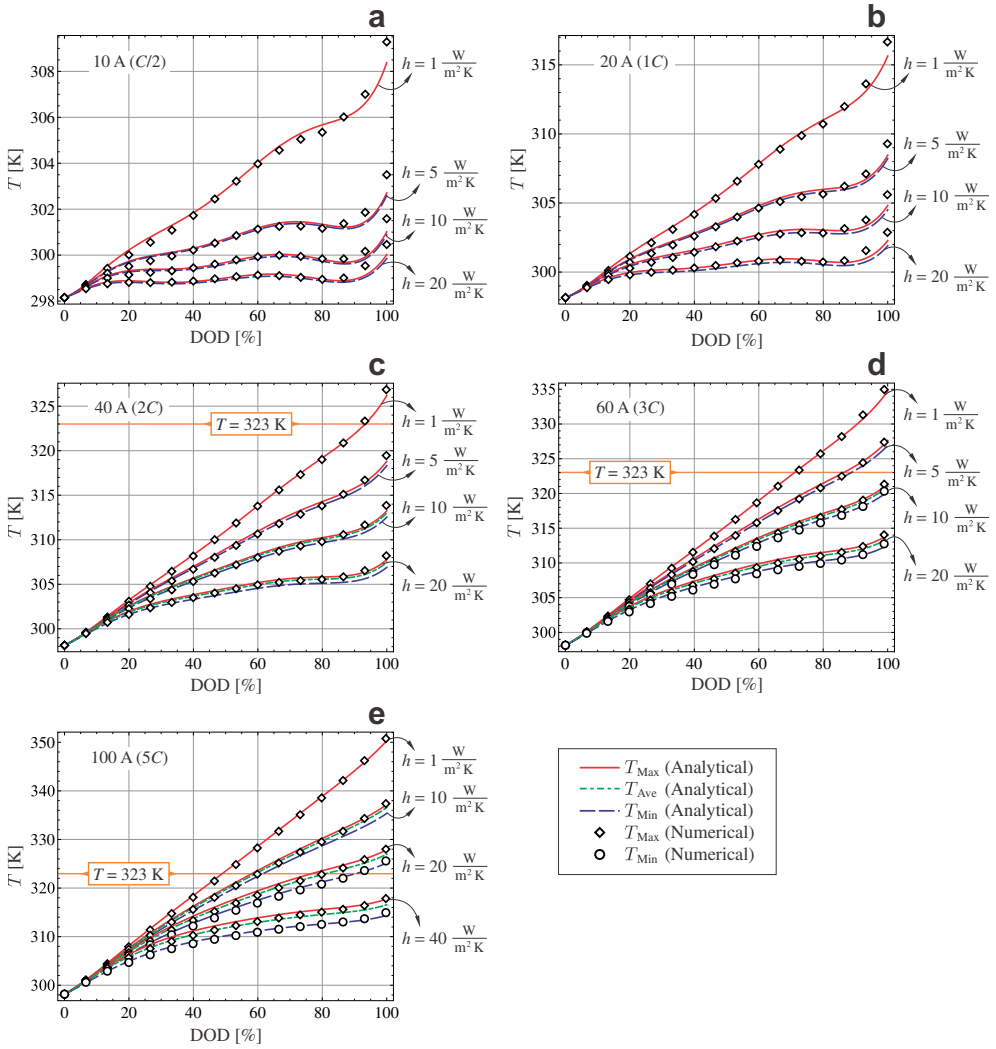

Fig. 5. Temperature variation vs. depth-of-discharge (DOD) is shown for different discharge rates. Maximum temperature at the battery center (red solid line), minimum temperature at the battery corner (blue long-dashed line), and average temperature (green dot-dashed line) are compared to numerical data for maximum temperature (diamond symbols ◇) and minimum temperature (circular symbols ○). In plots (a)–(d), thermal response of the battery during 10 A, 20 A, 40 A, and 60 A discharge currents is shown for $h_{ij} = \{1, 5, 10, 20\}$ W m^{-2} K^{-1}. For the case of 100 A discharge current (plot e), higher heat transfer coefficients are examined to lower the temperature below the critical temperature $T_{Cri} = 323.15$ K. (For interpretation of the references to color in this figure legend, the reader is referred to the web version of this article.)

coefficients are compared to numerical results from COMSOL Multiphysics finite element package (Version 4.2a). The comparison shows a good agreement between the analytical and numerical results. In numerical calculation the relative tolerance was set to 10^{-4}. The presented analytical results are obtained using only the first eigenvalue in each direction, which means the temperature is calculated only from the leading term of Eqs. (15) and (16),

$$T(\xi_1,\xi_2,\xi_3,\tau) = T_0 + \psi(\lambda_{11},\xi_1)\cdot\psi(\lambda_{21},\xi_2)\cdot\psi(\lambda_{31},\xi_3) \cdot\overline{\theta}(\lambda_{11},\lambda_{21},\lambda_{31},\tau), \tag{27}$$

with,

$$\overline{\theta}(\lambda_{11},\lambda_{21},\lambda_{31},\tau) = \int_{\xi_1'=0}^{1}\int_{\xi_2'=0}^{1}\int_{\xi_3'=0}^{1} \psi(\lambda_{11},\xi_1')\cdot\psi(\lambda_{21},\xi_2') \cdot\psi(\lambda_{31},\xi_3')\cdot\theta(\xi_1',\xi_2',\xi_3',\tau)\cdot d\xi_1'\cdot d\xi_2'\cdot d\xi_3'. \tag{28}$$

Inclusion of more terms from the series solution is expected to improve the accuracy of the analytical results. Indeed, our

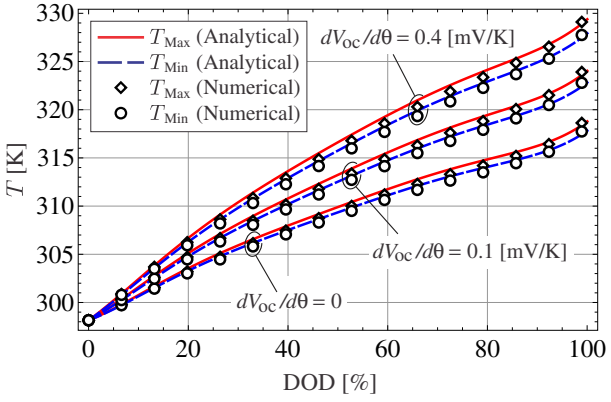

Fig. 6. Minimum and maximum temperature rise are shown for $dV_{oc}/d\theta = \{0, 0.1, 0.4\}$ mV K^{-1} during a 60 A discharge with $h_{ij} = 10$ W m^{-2} K^{-1}. Analytical results (lines) are compared to numerical data (symbols).

calculations confirm that series solutions up to 5 terms provide a better matching with the numerical data, particularly for large Biot numbers. Further increase of the terms in the series solution makes its computational cost to be comparable with numerical solution, while improvements in the results are negligible.

Thermal behavior of an adiabatic battery is approximated by setting $h_{ij} = 1$ W m^{-2} K^{-1}, while $h_{ij} = \{5, 10\}$ W m^{-2} K^{-1} represent natural-convection cooling effects. Higher value of h_{ij} represents forced-convection cooling. Plots (a) and (b) in Fig. 5 show that for 10 A and 20 A discharge rates, cell temperature does not reach to the critical temperature of $T_{Cri} = 323.15$ K, and natural-convection cooling suffices to limit the temperature rise below 7 K. However, as shown in plots (c)–(e), for 40 A, 60 A, and 100 A discharge currents, thermal runaway might initiate in the cell as its temperature exceeds the critical temperature. To avoid overheating of the battery in such cases, minimum heat transfer coefficients of $h = 5$ W m^{-2} K^{-1}, $h = 10$ W m^{-2} K^{-1}, and $h = 40$ W m^{-2} K^{-1} must be respectively applied to guarantee safe performance of the battery. The difference between T_{Max} and T_{Min} increases when higher rates of heat generation and surface heat dissipation are applied. In design of batteriy thermal management systems such temperature non-uniformities are preferred to be avoided, as they accelerate the rate of batteries degradation.

Throughout the results, T_{Ave} is closer to T_{Max} rather than T_{Min}. This trend which is more visible in Fig. 5(e) indicates that due to low thermal conductivity of the battery bulk, low temperature regions are limited to a small portion of the battery volume, i.e., corners (for more details see Fig. 7).

As given in Eq. (14b), the coefficient $dV_{oc}/d\theta$, dictated by battery chemistry [31], can significantly alter the magnitude of heat generation rate. In Fig. 6, increase of T_{Min} and T_{Max} are shown for $dV_{oc}/d\theta = \{0, 0.1, 0.4\}$ mV K^{-1}, while battery is discharged at 3C-rate (60 A) and subjected to cooling heat transfer coefficient of $h_{ij} = 10$ W m^{-2} K^{-1}.

When $T_{Max} - T_{Max}$ is small, one can use a lumped thermal model [32,33] to approximate the thermal behavior of the battery. Conventionally, Biot number is used to indicate the applicability of lumped thermal models; a Biot number less than 0.1 typically indicates a less than 5% error due to the lumped model assumption [34].

We define a surface-averaged Biot numbers for the battery,

$$\mathrm{Bi}_{\mathrm{Ave}} = \frac{1}{A}\sum_{i=1}^{3}\sum_{j=1}^{2}\mathrm{Bi}_{ij}A_{ij}, \tag{29}$$

where A is the total battery surface area, and A_{ij} is the area of the surface normal to x_i direction; $j = 0$ and $j = 1$ denote the surface at $x_i = 0$ and $x_i = L_i$, respectively. Biot number Bi_{ij} characterizes the ratio of convective heat transfer to conduction heat transfer at A_{ij} surfaces. Since thermal conductivity and dimensions of the battery are invariant, the only parameter affecting Bi_{ij} is h_{ij}. In Table 3, Biot numbers for some cases are listed. The surface-averaged Biot number suggests that for $h < 15$ W m^{-2} K^{-1} at all surfaces, a lumped thermal model is acceptable since $\mathrm{Bi}_{\mathrm{Ave}} < 0.1$. For forced-convective cases with $h > 15$ W m^{-2} K^{-1} a multi-dimensional approach must be applied as $\mathrm{Bi}_{\mathrm{Ave}} > 0.1$; however, since Biot number in x_2 direction is always less than the other two directions (see Table 3), a two-dimensional model in x_1–x_3 plane is also acceptable. Note that increasing of h in x_2 direction can change the

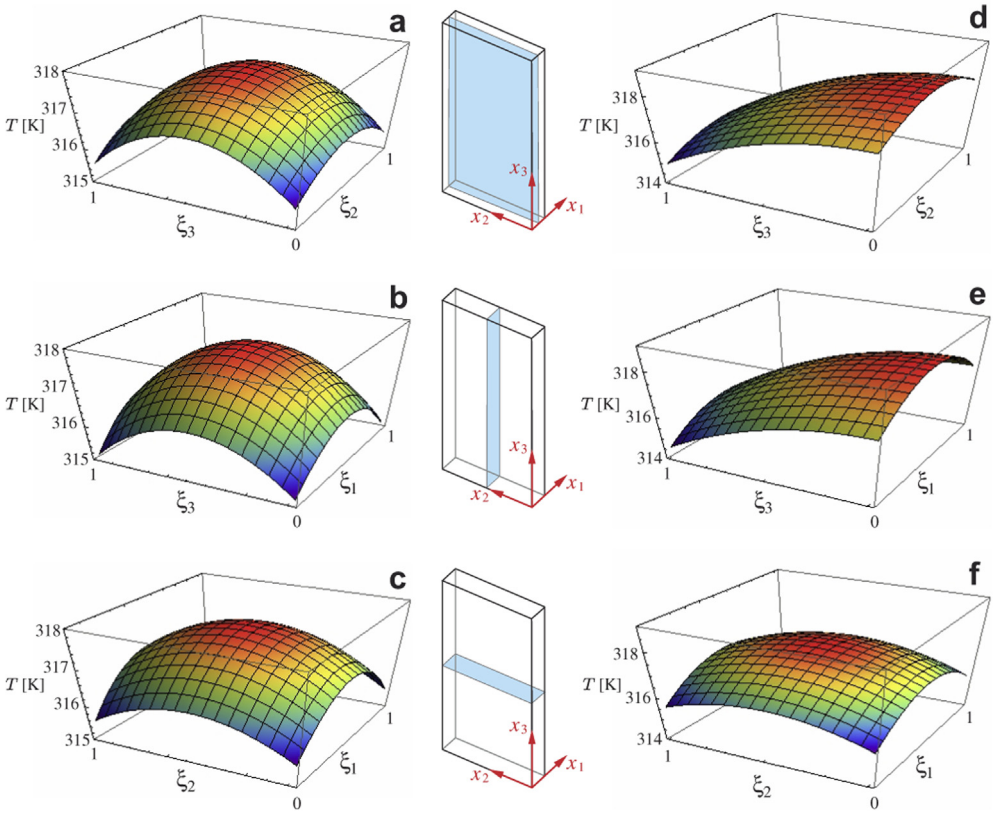

Fig. 7. In plots (a)–(c) temperature distribution at the end of 100 A discharge process is shown for $h_{ij} = 40$ W m^{-2} K^{-1} at all surfaces of the battery. In plots (d)–(f) temperature distribution at the end of 100 A discharge process is shown for $h_{31} = 1$ W m^{-2} K^{-1} and $h_{ij} = 40$ W m^{-2} K^{-1} for other surfaces. Ambient and initial temperature of 293.15 K was assumed. As a result of the system transformation, the results are mapped into a square region.

Table 3
Directional surface-averaged Biot numbers.

Heat transfer coefficient [W m^{-2} K^{-1}]	Bi_{1j}	Bi_{2j}	Bi_{3j}	Bi_{Ave}
$h = 5$	0.036	0.023	0.037	0.035
$h = 10$	0.072	0.047	0.073	0.071
$h = 15$	0.108	0.070	0.110	0.106
$h = 20$	0.144	0.094	0.147	0.141
$h = 30$	0.216	0.141	0.220	0.213
$h = 40$	0.289	0.188	0.293	0.284

choice for a two-dimensional model. Our criterion for a proper choice of a two-dimensional model is that it should capture both minimum and maximum temperatures in the battery. The analysis of averaged Biot number and its application to simplify the thermal problem is valid only for a homogeneous heat generation.

In Fig. 7, temperature distribution at the end of a 100 A discharge process is shown on $\xi_1 = 1/2$, $\xi_2 = 1/2$, and $\xi_3 = 1/2$ planes. Plots (a)–(c) show the temperature distribution when $h_{ij} = 40$ W m^{-2} K^{-1} is applied on all boundaries. Plots (d)–(f) correspond to the case in which $h_{31} = 1$ W m^{-2} K^{-1}, and on other surfaces $h_{ij} = 40$ W m^{-2} K^{-1}. The latter case is defined to examine the effects of non-uniform boundary conditions on the temperature distribution. In practical applications, indeed, at one side of the battery that is used for electrical connections, heat transfer coefficient differs from other sides (usually less). As a result of system transformation, i.e., Eq. (8), the solutions are mapped into a square region. A simple backward transformation can be used to remap the solutions into the original physical dimensions.

Plots (a)–(c) in Fig. 7 have the maximum temperature rise of $T_{Max} = 317.7$ K, whereas the minimum temperature rise exists at the corners of ξ_1–ξ_3 plane. This confirms the result of Biot number analysis, i.e., the best geometry choice for a two-dimensional modeling is a x_1–x_3 surface. This argument applies also for plots (d)–(f).

Finally, it should be emphasized that experimental observations as reported in Ref. [27] show that maximum temperature in our sample battery occur in the vicinity of battery tabs, where current density, and thus, Joulean heat generation are maximum. Since our thermal model is not coupled with an electrical model, this phenomenon is not discussed here.

5. Conclusion

Based on the method of integral-transformation, a closed-form analytical model is developed to describe temperature distribution in batteries with modest numerical effort. The proposed thermal model takes account for:

- multi-dimensional heat conduction,
- orthotropic thermal conductivities,
- time dependent and temperature dependent heat generation terms,
- convective–radiative boundary conditions,

and hence provide a useful tool for investigating the thermal behavior of batteries in various operating conditions. The accuracy of the model was confirmed through comparison with numerical data.

The proposed model was employed to study the temperature rise in a prismatic Li-ion polymer cell during discharge processes, where transient heat generation rate was approximated from the electrical performance of the battery. The results showed that for the considered battery, natural convection can prevent battery overheating during low and moderate discharge processes, when a room temperature (25 °C) was considered as the initial and ambient temperatures. For more aggressive discharge conditions higher heat transfer rates at battery surface are required, e.g., forced-convection or liquid cooling. Certain conditions, under which a two-dimensional thermal analysis is applicable, are highlighted through definition of a surface-averaged Biot number.

In large battery assemblies the issue of temperature rise becomes more critical, as heat accumulates at the center of the battery module. Indeed, adaptation of the proposed method to battery modules is a straightforward task, for which other practical and engineering consideration such as thermal contact resistances between different components of the assembly, i.e., battery cells and module case, should be considered. Furthermore, the presented procedure can be used to investigate the thermal behavior of batteries, particularly Li-ion and NiMH batteries, during cyclic loads [35].

To conclude, it is important to highlight the major limit of the proposed thermal model which is the necessity of linear boundary conditions. This limit that is dictated by the Sturm–Liouville theory, implies that heat transfer coefficient h must be constant on the surface. In reality, the convective heat transfer coefficient h varies over battery surfaces, due to formation of boundary layers. The effects of nonlinear boundary conditions on the thermal behavior of Li-ion batteries are discussed in Ref. [19].

Acknowledgment

This work was financially supported by Automotive Partnership Canada (APC), Grant No. APCPJ 401826-10.

Appendix A. Details of the thermal model implementation

The analytical thermal model is formulated in Section 3, and in this section, the required calculations to implement the model are explained and listed in order.

The dimensions of the battery $\{L_1, L_2, L_3\}$, and thermophysical properties $\{\rho, c_p, \kappa_1, \kappa_2, \kappa_3\}$ of the battery components are the inputs for the model, as listed in Tables 1 and 2. Effective thermophysical properties of the battery must be calculated in accordance to Eqs. (24) and (25). Moreover, the entropic heat generation coefficient dV_{oc}/dT is known from measurements or electrochemical simulations. Initial temperature of the battery and the temperature of environment T_0, and the convective–radiative heat transfer coefficient h_{ij} need to be provided to define different scenarios.

According to Eq. (7), the entropic heat generation inside the battery depends on temperature. However, the irreversible part of heat generation, which turns out to be a function of time only, can be calculated from the voltage response of the battery during discharge processes [cf. Fig. 3].

After transforming Eqs. (1), (3), (6) and (7) into Eqs. (9), (11), (10), and (14) the following calculations must be performed in order.

1. Calculate $G_{rev} + G_0$versus τ from Eq. (14b). For this, voltage response of the battery during the discharge process must be used.
2. Solve Eq. (20) to find a finite list of eigenvalues in each direction $\boldsymbol{\lambda}_i = \{\lambda_1, \lambda_2, \lambda_3, \ldots\}_i$.
3. From Eq. (21) find a normalization factor for each eigenvalue $\boldsymbol{\eta}_i = \{\eta_1, \eta_2, \eta_3, \ldots\}_i$.
4. Use Eq. (18) to define eigenfunctions $\phi(\boldsymbol{\lambda}_i, \xi_i)$ based on the eigenvalues calculated in step 2.
5. Use Eq. (17) and the results of steps 3 and 4 to find the transformation kernels $\psi(\boldsymbol{\lambda}_i, \xi_i)$.
6. Use Eq. (22c) and take the integral transform of $G_{rev} + G_0$ (see step 1).

7. Use the result of step 6 to construct the ODE in Eq. (22a). Note that the number of ODEs depends on the number of eigenvalues in each direction.
8. General solution for ODEs is given in Eq. (23). Adapt this solution for each ODE and find constants $\mathscr{C}$ from the initial conditions.
9. Replace the solutions for ODEs (step 8) into the inversion formula, Eq. (16), to find a series-form solution for temperature in dimensionless form $\theta(\xi_1, \xi_2, \xi_3, \tau)$.

References

[1] D. Linden, Handbook of Batteries, second ed., McGraw-Hill, New York, 1995.
[2] K. Lee, J. Power Sources 132 (2004) 201–205.
[3] S. Szpak, C.J. Gabriel, J.R. Driscoll, Electrochim. Acta 32 (1987) 239–246.
[4] B. Mandal, A. Padhi, Z. Shi, S. Chakraborty, R. Filler, J. Power Sources 162 (2006) 690–695.
[5] A.K. Thapa, G. Park, H. Nakamura, T. Ishihara, N. Moriyama, T. Kawamura, H. Wang, M. Yoshio, Electrochim. Acta 55 (2010) 7305–7309.
[6] S.S. Zhang, Electrochem. Commun. 4 (2002) 928–932.
[7] Y. Inui, Y. Kobayashi, Y. Watanabe, Y. Watase, Y. Kitamura, Energy Convers. Manag. 48 (2007) 2103–2109.
[8] S. Al-Hallaj, J.R. Selman, J. Power Sources 110 (2002) 341–348.
[9] G.-H. Kim, A. Pesaran, R. Spotnitz, J. Power Sources 170 (2007) 476–489.
[10] G.G. Botte, V.R. Subramanian, R.E. White, Electrochim. Acta 45 (2000) 2595–2609.
[11] T.M. Bandhauer, S. Garimella, T.F. Fuller, J. Electrochem. Soc. 158 (2011) R1–R25.
[12] C.R. Pals, J. Newman, J. Electrochem. Soc. 142 (1995) 3274–3281.
[13] Y. Chen, J. Electrochem. Soc. 140 (1993) 1833.
[14] L. Song, J.W. Evans, J. Electrochem. Soc. 145 (1998) 2327–2334.
[15] K.H. Kwon, C.B. Shin, T.H. Kang, C.-S. Kim, J. Power Sources 163 (2006) 151–157.
[16] J. Lee, K.W. Choi, N.P. Yao, C.C. Christianson, J. Electrochem. Soc. 133 (1986) 1286–1291.
[17] Y. Chen, J.W. Evans, J. Electrochem. Soc. 141 (1994) 2947–2955.
[18] Y. Chen, J.W. Evans, J. Electrochem. Soc. 143 (1996) 2708–2712.
[19] S.C. Chen, C.C. Wan, Y.Y. Wang, J. Power Sources 140 (2005) 111–124.
[20] J. Newman, W. Tiedemann, J. Electrochem. Soc. 142 (1995) 1054–1057.
[21] M.N. Özisik, Boundary Value Problems of Heat Conduction, Dover Publications, New York, 1989.
[22] H.S. Carslaw, J.C. Jaeger, Conduction of Heat in Solids, second ed., Clarendon Press, Oxford, 1959.
[23] G.G. Botte, B.A. Johnson, R.E. White, J. Electrochem. Soc. 146 (1999) 914–923.
[24] M. Doyle, T.F. Fuller, J. Newman, J. Electrochem. Soc. 140 (1993) 1526–1533.
[25] D. Bernardi, E. Pawlikowski, J. Newman, J. Electrochem. Soc. 132 (1985) 5–12.
[26] L. Rao, J. Newman, J. Electrochem. Soc. 144 (1997) 2697–2704.
[27] U.S. Kim, C.B. Shin, C.-S. Kim, J. Power Sources 180 (2008) 909–916.
[28] U.S. Kim, C.B. Shin, C.-S. Kim, J. Power Sources 189 (2009) 841–846.
[29] P. Taheri, S. Hsieh, M. Bahrami, J. Power Sources 196 (2011) 6525–6533.
[30] R. Sabbah, R. Kizilel, J.R. Selman, S. Al-Hallaj, J. Power Sources 182 (2008) 630–638.
[31] Y. Ye, Y. Shi, N. Cai, J. Lee, X. He, J. Power Sources 199 (2012) 227–238.
[32] P. Nelson, I. Bloom, K. Amine, G. Henriksen, J. Power Sources 110 (2002) 437–444.
[33] K. Smith, C.-Y. Wang, J. Power Sources 160 (2006) 662–673.
[34] F.P. Incropera, D.P. DeWitt, T.L. Bergman, A.S. Lavine, Fundamentals of Heat and Mass Transfer, sixth ed., John Wiley & Sons, New York, 2007.
[35] S. Chacko, Y.M. Chung, J. Power Sources 213 (2012) 296–303.

Nomenclature

A: total surface area (m^2)
A_{ij}: areas of individual surfaces (m^2)
Bi_{ij}: Biot numbers at individual surfaces
Bi_{Ave}: surface-averaged Biot number
c_p: heat capacity (J kg^{-1} K^{-1})
g: total heat generation rate (W m^{-3})
G: total source for temperature rise (K)
G_0: source for temperature rise due to initial temperature (K)
G_{irrev}: irreversible source for temperature rise (K)
G_{rev}: reversible source for temperature rise (K)
h_{ij}: combined heat transfer coefficients at individual surfaces (W m^{-2} K^{-1})
$h_{c,ij}$: convective heat transfer coefficients at individual surfaces (W m^{-2} K^{-1})
$h_{r,ij}$: radiative heat transfer coefficients at individual surfaces (W m^{-2} K^{-1})
I: battery charge/discharge current (A)
K_i: dimensionless thermal conductivity in x_i direction
ℓ_j: thickness of the jth layer in battery core (m)
L_i: dimension of battery core in x_i direction (m)
N: number of layers in battery core
$q_{c,ij}$: convective heat fluxes at individual surfaces (W m^{-2})
$q_{r,ij}$: radiative heat fluxes at individual surfaces (W m^{-2})
t: time (s)
T: core temperature (K)
T_0: ambient and initial temperatures (K)
T_{ij}: temperatures at individual surfaces (K)
V: operational battery voltage (V)
V_{oc}: open circuit potential (V)
$\mathscr{V}$: volume (m^3)
$\mathscr{V}_j$: volume of the jth layer in battery core (m^3)
x_i: position in Cartesian coordinate system (m)
BTMS: battery thermal management system
DOD: depth-of-discharge
H/PEV: hybrid and plug-in electric vehicle
Li-ion: lithium-ion
NiMH: nickel–metal hydride
OCP: open circuit potential

Greek
ε: emissivity of surface
$\boldsymbol{\eta}_i$: normalization factors for eigenfunctions in x_i direction
θ: core temperature rise (K)
θ_{ij}: temperature rise at individual surfaces (K)
κ_i: thermal conductivity in x_i direction (W m^{-1} K^{-1})
$\boldsymbol{\lambda}_i$: eigenvalues in x_i direction
ξ_i: dimensionless position in Cartesian coordinate system
ρ: mass density (kg m^{-3})
σ: Stefan–Boltzmann constant (W m^{-2} K^{-4})
τ: dimensionless time
ϕ: eigenfunction
ψ: transformation kernel

Superscript
$\bar{}$: transformed quantity based on Eq. (15)